

Trimer Dynamics in Floquet-driven arrays of Rydberg Atoms

Edoardo Tiburzi,^{1,2} Lorenzo Maffi,^{1,2} Luca Dell'Anna,^{1,2,3} and Marco Di Liberto^{1,2,3}

¹*Dipartimento di Fisica e Astronomia “G. Galilei”,*

Università degli Studi di Padova, I-35131, Padova, Italy

²*INFN Istituto Nazionale di Fisica Nucleare, Sezione di Padova, I-35131, Padova, Italy*

³*Padua Quantum Technologies Research Center (QTECH), Padova, Italy*

We analyze the WAHUHA Floquet protocol recently applied to arrays of Rydberg atoms and derive beyond-leading-order corrections in the high-frequency expansion of the effective spin theory. We find that an appropriate choice of the pulses times can enforce an approximate symmetry corresponding to the conservation of the total magnetization. The interaction channels emerging from higher-order Floquet terms affect three-body bound states (*trimers*), which gain a significant mobility. We estimate the corresponding enhancement in 1D spin chains and conclude that their dynamics is within experimental reach. Detrimental effects due to the proliferation of particles outside of the trimer magnetization sector are found to occur and spread on time-scales slower than the trimer propagation. Moreover, these can be suppressed in higher dimensional lattices, e.g. in 2D triangular lattices, as the lattice geometry brings these processes off resonance. Our results establish a concrete route to realizing mobile multiparticle bound states in Floquet-engineered Rydberg platforms.

I. INTRODUCTION

Spin models provide a paradigmatic framework to describe many-body systems [1]. Recent developments in quantum simulation platforms have opened avenues for their programmable realization with tunable interactions and geometries [2]. In this context, spin models have been employed to capture effective quantum properties of systems described by Hubbard models, for example, with ultracold mobile atoms [3–7]. Furthermore, they emerge as main description for arrays of long-range interacting atoms, as dipolar atoms and polar molecules [8, 9], or Rydberg atoms [10, 11]. In particular, strong Rydberg-Rydberg interactions have enabled the experimental realization of paradigmatic spin-1/2 Hamiltonians, such as the Ising, XY, and XXZ models, in one and two dimensions by encoding the spin degree of freedom in a pair of atomic levels [12].

These long-range interacting systems have made possible to explore the ground state properties of spin models, including quantum phase transitions [13, 14], topological states [15, 16] and low-energy excitations, for example, single magnons, collective excitations or domain walls [17, 18]. In this context, bound states can also appear in the excitation spectrum [4, 19–23] at the cost of a slower time evolution due to their higher mass. Two-particle bound states have been largely investigated with synthetic matter systems with onsite interactions, as for the case of Hubbard models [24, 25]. Systems with long-range interactions however display distinct features. They can manifest a critical interaction strength for the existence of stable bound states [26], recently observed with Rydberg dressed bosonic atoms [27]. The interplay of long-range strong interactions and lattice geometry can lead to bound states with emergent topological or localization properties absent in the noninteracting regime [28, 29]. Recently, more complex bound states or excitations, like string excitations or domain walls [30–33]

have been the focus of investigation due to their exotic dynamical properties, including the connection to gauge theories and confinement [34].

While native models of the atomic platform already provide a rich playground to study spin models and their few particle or collective excitations, it is crucial to design schemes that allow a higher degree of control of these many-body systems. Floquet engineering has emerged as a versatile method to manipulate atomic systems and their quantum Hamiltonians via time-dependent periodic drives [35, 36]. In the case of mobile ground state atoms, Floquet techniques have been employed to control many-body transport properties across phase transitions [37, 38], engineer gauge fields [39–41], induce topological band structures [42–44] and design interacting models [45, 46]. In the context of Rydberg atoms, recent progress has shown that Floquet methods can conveniently be employed to manipulate interactions beyond the limitations of the native models [47, 48], for example to engineer the Kitaev honeycomb model and its non-Abelian topological properties [49–51]. A particularly convenient driving scheme, known as WAHUHA pulse sequence [52], has been employed to engineer the XYZ Hamiltonian [53, 54] at leading order in the Floquet high-frequency expansion. Tunability of time pulses allows to tune the model in a parameter region where magnetization is conserved. In this regime, the model exhibits an $SO(2)$ symmetry and is described by an XXZ spin model that can be tuned to the rotational invariant Heisenberg limit. However, beyond-leading-order corrections are expected, in general, to generate a proliferation of spin-spin interaction terms that can break this symmetry.

In this work, we investigate the WAHUHA protocol for long-range interacting Rydberg atoms described by the XY model. We derive next-to-leading order Floquet corrections up to order $1/\omega^2$, with ω the driving frequency, and we find a regime of pulse times that removes all terms

violating the conservation of magnetization except for one. We then study their impact on the dynamics of three-body bound states (*trimers*) [29, 55, 56]. Three-particle bound states are expected to have a very large mass in the XXZ model, which hinders the possibility of observing them in experiments. Here we show that WAHUHA Floquet engineering provides additional channels that significantly increase the mobility of trimers. We also investigate the role of long-range couplings showing that they contribute positively to the trimer mobility. Moreover two-dimensional lattice geometries can help mitigating the proliferation of states from other unwanted magnetization sectors. Our findings highlight the potential of Floquet-engineered Rydberg systems for studying exotic few-body excitations and correlated dynamics in strongly-interacting quantum matter.

The paper is organized as follows. In Sec. II we introduce the WAHUHA Floquet driving protocol and derive the corresponding effective Hamiltonian up to second order in the high-frequency expansion. We then specialize to a one-dimensional chain with nearest-neighbor couplings and choose the pulse durations such as to enforce an approximate $SO(2)$ symmetry. In this regime, the effective Hamiltonian acquires a particularly transparent form, in which different contributions can be directly identified as nearest- and next-nearest-neighbor hopping, correlated hopping and multisite processes, making their impact on the mobility of magnons, dimers and trimers explicit. In Sec. III we discuss the formation and dynamics of three-body bound states (trimers) in one-dimensional chains, and analyze how the Floquet-induced terms modify their dispersion and propagation compared to magnons and dimers. In Sec. IV we extend our analysis to systems with long-range interactions and to two-dimensional lattice geometries, showing how these ingredients enhance trimer mobility and at the same time suppress unwanted mixing between different magnetization sectors. Finally, in Sec. V we summarize our results and outline perspectives for experimental implementations and future developments. Technical details on the Floquet expansion and on the structure of the effective couplings are collected in the Appendices.

II. WAHUHA FLOQUET DRIVING

A. Effective theory: Leading order

We study the Floquet dynamics of a periodically driven spin system described by the Hamiltonian:

$$H_{\text{driven}} = H_{\text{XY}} + W(t), \quad (1)$$

where

$$H_{\text{XY}} = \frac{1}{2} \sum_{i \neq j} J_{ij} (\sigma_i^x \sigma_j^x + \sigma_i^y \sigma_j^y), \quad (2)$$

is the native XY Hamiltonian of the spin system at hand, for example arising from dipolar couplings be-

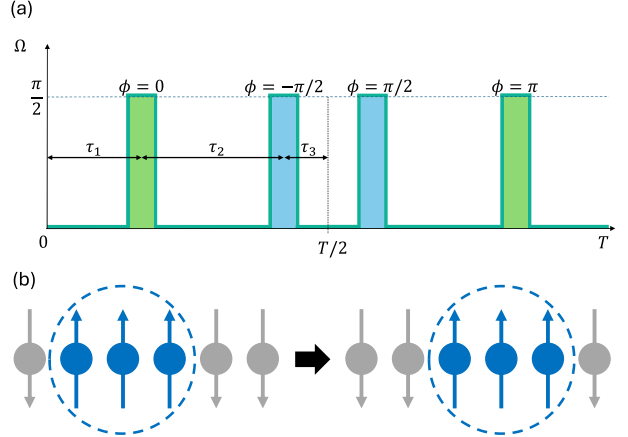


Figure 1: Floquet pulse scheme and trimer dynamics. (a) Schematic representation of the WAHUHA Floquet driving sequence, consisting of four $\pi/2$ pulses applied at times t_1, t_2, t_3, t_4 with phases $\phi = 0, -\pi/2, \pi/2, \pi$, separated by intervals $\tau_1, \tau_2, 2\tau_3$, such that $\tau_1 + \tau_2 + \tau_3 = T/2$. This protocol effectively engineers anisotropic spin interactions by averaging out undesired terms. (b) Illustration of a trimer (three adjacent spin excitations forming a bound state) propagating coherently along a one-dimensional spin chain.

tween Rydberg atoms [11]. The periodic drive $W(t)$ follows the WAHUHA protocol [52–54], notably realized by the sequence of four $\pi/2$ pulses with fixed phases $\phi = \{0, -\pi/2, \pi/2, \pi\}$ and separated by time intervals $\tau_1, \tau_2, 2\tau_3$ such that $\tau_1 + \tau_2 + \tau_3 = T/2$, with T being the driving period (see Fig. 1(a)).

In the rotating frame defined by the explicit form of the drive

$$W(t) = \frac{\hbar\Omega(t)}{2} \sum_i [\cos \phi(t) \sigma_i^x + \sin \phi(t) \sigma_i^y], \quad (3)$$

the Hamiltonian becomes:

$$\begin{aligned} H'(t) &= U_{\text{drive}}^\dagger(t) H_{\text{driven}} U_{\text{drive}}(t) - i\hbar U_{\text{drive}}^\dagger(t) \frac{dU_{\text{drive}}(t)}{dt} \\ &= U_{\text{drive}}^\dagger(t) H_{\text{XY}} U_{\text{drive}}(t), \end{aligned} \quad (4)$$

where $U_{\text{drive}}(t) = \mathcal{T} e^{-\frac{i}{\hbar} \int_0^t d\tau W(\tau)}$ is the time-evolution operator. According to standard Floquet theory [35, 36] (see Appendix A) we can describe the effective dynamical behaviour of the system by a systematic high-frequency expansion in $\omega \equiv 2\pi/T$ leading to a time-independent effective Hamiltonian H_{eff} . At leading order, we obtain

$$H_{\text{eff}} = \sum_n \frac{1}{\omega^n} H_{\text{eff}}^{(n)} \approx H_0 + \mathcal{O}(1/\omega^2), \quad (5)$$

where H_0 was studied in Refs. [53, 54] and it is given by:

$$\begin{aligned} H_0 &= \sum_{i \neq j} \frac{J_{ij}}{T} [(\tau_1 + \tau_2) \sigma_i^x \sigma_j^x + (\tau_1 + \tau_3) \sigma_i^y \sigma_j^y \\ &\quad + (\tau_2 + \tau_3) \sigma_i^z \sigma_j^z]. \end{aligned} \quad (6)$$

The results above show that this Floquet protocol provides a flexible scheme for engineering a generic XYZ spin model. By tuning the times τ_1 , τ_2 and τ_3 , it is possible to obtain different regimes. When $\tau_2 = \tau_3$, the model preserves $SO(2)$ with respect the z axis and conserves magnetization. Moreover, for $\tau_1 = \tau_2 = \tau_3$ the model reduces to the celebrated Heisenberg model with $SO(3)$ rotational invariance. In the following, we investigate the higher-frequency corrections of this model, which were neglected in previous analyses.

B. Effective theory: Correction $1/\omega^2$

As detailed in Appendix A and B, the first non-vanishing correction to H_0 arises at the second-order in the Floquet perturbative expansion (5), and takes the form $H_{\text{eff}}^{(2)}/\omega^2 = H^{2\sigma} + H^{4\sigma}$ where $H^{2\sigma}$ and $H^{4\sigma}$ respectively correspond to two-spin and four-spin coupling terms explicitly given by

$$H^{2\sigma} = \sum_{j>k} \left(\mathcal{J}_{j,k}^x \sigma_j^x \sigma_k^x + \mathcal{J}_{j,k}^y \sigma_j^y \sigma_k^y + \mathcal{J}_{j,k}^z \sigma_j^z \sigma_k^z \right), \quad (7)$$

and

$$H^{4\sigma} = \sum_{\substack{h>i \\ j>k}}' \left(C_{hi;jk}^{yz} \sigma_h^y \sigma_i^y \sigma_j^z \sigma_k^z + C_{hi;jk}^{zx} \sigma_h^z \sigma_i^z \sigma_j^x \sigma_k^x \right. \\ \left. + C_{hi;jk}^{xy} \sigma_h^x \sigma_i^x \sigma_j^y \sigma_k^y \right), \quad (8)$$

where the restricted summation $\sum'(\dots)$ excludes terms with $(h,i) = (j,k)$.

The Hamiltonian $H_{\text{eff}}^{(2)}$ does not possess in general any explicit relevant symmetry except for the trivial \mathbb{Z}_2 parity ($\vec{\sigma} \rightarrow -\vec{\sigma}$). However, under certain conditions an approximate $SO(2)$ symmetry emerges. In particular, when $\tau_2 = \tau_3$ and $\tau_1 \ll \tau_2, \tau_3$ the two-spin and four-spin couplings satisfy $\mathcal{J}_{j,k}^x = \mathcal{J}_{j,k}^y$ and $C_{hi;jk}^{yz} = C_{jk;hi}^{zx}$. Explicit $SO(2)$ symmetry breaking originates exclusively from terms of the form $\sigma_h^x \sigma_i^x \sigma_j^y \sigma_k^y$ which reduce the symmetry to the \mathbb{Z}_4 subgroup of rotations by $\pi/2$ around the z axis. In turn, the limit $\tau_1 = 0$ corresponds to having the first and last pulse of the WAHUHA sequence to coincide in time. As you can easily inspect from Eq. (3) this condition of having two identical pulses to coincide is equivalent to the identity operator. In the rest of the manuscript, we will consider a simplified WAHUHA sequence corresponding to second and third pulses in Fig. 1(a) with $\tau_2 = \tau_3 = T/4$ with a rotation around the y axis.

In order to simplify our discussion, we limit ourselves for the moment to nearest-neighbor J_{ij} couplings in Eq. (2) and we fix the lattice to be a one-dimensional chain. Under these assumptions, the Hamiltonian reads $H_{\text{eff}} \approx H_{\text{eff}}^{(0)} + H_{\text{eff}}^{(2)}/\omega^2 = H_{SO(2)} + H_{SO(2)}$, where the two

terms take the form

$$H_{SO(2)} = \\ (1 - \Gamma) \sum_i (\sigma_i^+ \sigma_{i+1}^- + \sigma_i^- \sigma_{i+1}^+ + \sigma_i^z \sigma_{i+1}^z) \\ + \Gamma \sum_i (\sigma_i^+ \sigma_{i+2}^- + \sigma_i^- \sigma_{i+2}^+ - \sigma_i^z \sigma_{i+2}^z) \\ - \Gamma \sum_i (\sigma_{i-1}^z \sigma_{i+1}^z + \sigma_{i+1}^z \sigma_{i+3}^z) (\sigma_i^+ \sigma_{i+2}^- + \sigma_i^- \sigma_{i+2}^+) \quad (9) \\ + 2\Gamma \sum_i \sigma_{i+1}^z \sigma_{i+2}^z (\sigma_i^+ \sigma_{i+3}^- + \sigma_i^- \sigma_{i+3}^+) \\ + 2\Gamma \sum_i (\sigma_i^+ \sigma_{i+1}^+ \sigma_{i+2}^- \sigma_{i+3}^- + \sigma_i^- \sigma_{i+1}^- \sigma_{i+2}^+ \sigma_{i+3}^+),$$

and

$$H_{SO(2)} = -2\Gamma \sum_i \sigma_i^+ \sigma_{i+1}^+ \sigma_{i+2}^+ \sigma_{i+3}^+ + \text{h.c.}, \quad (10)$$

assuming units $J_{nn} \equiv J_{i,i+1} = 1$. As it is evident from the equations above, $H_{SO(2)}$ contains terms all of which conserve the total magnetization, while $H_{SO(2)}$ includes only a term violating this conservation law. Within Floquet perturbation theory we can readily obtain the coefficient $\Gamma \equiv \frac{1}{6} \left(\frac{J_{nn}\pi}{\omega} \right)^2$, as shown in App. B.

The symmetric Hamiltonian in Eq. (9) can be interpreted as a sum of distinct physical contributions. The first line represents the leading-order Hamiltonian, which is a nearest-neighbor XXZ model and includes higher-order Floquet corrections via Γ . The second line introduces longer-range corrections to the previous XXZ model proportional to Γ , including next-nearest-neighbor hopping and interactions. Starting from the third line, higher-order spin correlations appear. The third and fourth line describe correlated hopping processes whereas the fifth and last line corresponds to pair-hopping processes, in which two spins hop together across adjacent sites, effectively shifting a pair by two sites. Crucially, the emergent interactions described by the operator $\sigma_{i+1}^z \sigma_{i+2}^z (\sigma_i^+ \sigma_{i+3}^- + \sigma_i^- \sigma_{i+3}^+)$ are relevant for the mobility of trimers, as we will further discuss below. The resulting Floquet Hamiltonian dynamics has been benchmarked with the full exact dynamics in Appendix C for a range of parameters and timescales compatible with the results that we show below.

III. TRIMER DYNAMICS

In this section we investigate the dynamics of three-body bound states (hereafter referred to as trimers) in the effective models derived above. In the static nearest-neighbor XXZ chain such excitations are known to be very heavy, as their motion arises only through higher-order virtual processes. The Floquet-engineered Hamiltonian introduced in Sec. II instead contains additional hopping and correlated terms whose contribution to trimer motion becomes explicit in the simplified one-dimensional, nearest-neighbor setting adopted

here. We first recall the structure and dispersion of the trimer in the XXZ limit, and then analyze how Floquet corrections alter its mobility and its robustness against residual $SO(2)$ -breaking channels.

A. What is a trimer?

Consider a one-dimensional spin-1/2 XXZ model with nearest-neighbor interactions and closed boundary conditions described by the Hamiltonian

$$H = 2h \sum_i (\sigma_i^+ \sigma_{i+1}^- + \sigma_i^- \sigma_{i+1}^+) + \Delta \sum_i \sigma_i^z \sigma_{i+1}^z. \quad (11)$$

We focus on the ordered phase regime $|h/\Delta| < 1$ and $\Delta > 0$, where the Ising interaction dominates. The leading order term in the effective Hamiltonian (9) corresponds to the XXZ model for $h/\Delta = 0.5$.

For the purpose of studying the dynamics of spin-flip clusters, it is convenient to adopt the fully polarized state $|0\rangle = |\downarrow\downarrow\ldots\downarrow\rangle$ as a reference. Although this state corresponds to the highest energy configuration in the antiferromagnetic regime, it provides a simple and intuitive background in which flipped spins can propagate, interact, and form bound states. Within this picture, a single flipped spin $|i\rangle_S \equiv |\ldots\downarrow\downarrow i\downarrow\downarrow\ldots\rangle$ (i.e. a *magnon*) plays the role of a mobile particles, enabling a clean description of its dynamics. Two magnons can form bound states $|i\rangle_D \equiv |\ldots\downarrow\uparrow_i\uparrow_{i+1}\downarrow\ldots\rangle$, here dubbed dimers, with distinct energy than free magnons. The XXZ model also supports multiparticle bound states [4, 19, 22, 23] and here we consider the case of three adjacent spin flips: a “trimer” $|i\rangle_T = |\ldots\downarrow\uparrow_i\uparrow_{i+1}\uparrow_{i+2}\downarrow\ldots\rangle$.

The existence and stability of trimers can be understood perturbatively by considering the subspace of states $|i\rangle_T$ weakly coupled by the weak spin exchange term proportional to h . The effective low-energy Hamiltonian takes the form of a tight-binding model:

$$\mathcal{H}_T = \sum_i \epsilon_T |i\rangle \langle i| + t_T (|i+1\rangle \langle i| + \text{h.c.}), \quad (12)$$

where $|i\rangle \equiv |i\rangle_T$ denotes the trimer localized at sites $i, i+1, i+2$, ϵ_T is the on-site energy of the trimer state, t_T is the effective hopping amplitude. From perturbation theory, one finds:

$$\epsilon_T = E_0 + 2 \frac{h^2}{\Delta} + \mathcal{O}(h^4), \quad (13)$$

where $E_0 = (L-4)\Delta$ with L the number of sites of the chain with closed boundary conditions. The trimer hopping amplitude reads:

$$t_T = \frac{h^3}{2\Delta^2}, \quad (14)$$

where the only relevant virtual states are spin patterns of the form $|\ldots\downarrow\uparrow\downarrow\uparrow\uparrow\downarrow\ldots\rangle$ and $|\ldots\downarrow\uparrow\uparrow\downarrow\uparrow\downarrow\ldots\rangle$, whose

energy difference from the trimer manifold is 4Δ . From Eq. (12), the trimer dispersion relation reads:

$$E_T(k) = E_0 + 2 \frac{h^2}{\Delta} + \frac{h^3}{\Delta^2} \cos k. \quad (15)$$

It is important to emphasize that the trimer band described above represents only a subset of the full spectrum at fixed total magnetization $N_\uparrow = 3$, which is represented in Fig. 2(a). In this sector, one also finds states where the three spin-ups are not adjacent, such as configurations with two nearby spins and one separated (i.e. those used above for enabling the trimer mobility), or three completely separated spins. These configurations give rise to additional bands in the energy spectrum yielding bound state bands and scattering continua.

From a perturbative perspective, the coherent propagation of the trimer is well-defined as long as its band remains separated from the scattering states, namely for sufficiently small values of h . As h increases, the trimer band lowers in energy and eventually overlaps with the scattering continuum triggering conversion of trimers into lower-spin constituents (i.e. magnons and 2-magnon bound states)

A crucial ingredient for identifying trimers as coherent quasiparticles is the conservation of the total magnetization, i.e. an $SO(2)$ symmetry. As visible from the band structure in Fig. 2(b), the trimer band can overlap in energy to single-magnon states and other string-like excitations that share the same number of domain walls but differ in spin number, such as dimer bound states. Without magnetization conservation, such resonances would enable mixing between these sectors, obscuring the identification of trimers as coherent, long-lived modes.

Finally, it is worth noting that trimers move significantly much slower than other excitations. Their effective hopping amplitude arises at third order in perturbation theory via two virtual states, scaling as $t_T \sim h^3/\Delta^2$. In contrast, a single magnon propagates directly at first order in h , while a two-magnons bound state hops at second order with amplitude $\sim h^2/\Delta$. As a result, the trimer band appears almost flat compared to the others (Fig. 2(b)), and its group velocity is suppressed. This slow dynamics can be a limiting factor for experimental detection, since the trimer motion may occur over timescales longer than the coherence times of available platforms. This motivates the effort to identify schemes that allow to enhance its dynamics and visibility through suitable engineering of system parameters, as we discuss in this work and more specifically in the next paragraph.

B. Trimer dynamics and $SO(2)$ leakage

The propagation timescales of a trimer can be significantly enhanced by perturbations that introduce correlated longer-range hopping processes. A concrete example of such a modification is provided by the effective

model previously introduced in Eq. (9), where a small parameter $\Gamma \ll 1$ controls various next-nearest and higher-order spin interactions. In particular, the fourth line of Eq. (9) contains a correlated third-neighbor hopping term of the form $\Gamma \sigma_{i+1}^z \sigma_{i+2}^z (\sigma_i^+ \sigma_{i+3}^- + \sigma_i^- \sigma_{i+3}^+)$. This term directly enables a first-order coherent hopping process for the trimer as a whole, without the need of virtual intermediate steps (see Fig 2(c)). However such process will interfere with the ones originating from the rest of the Hamiltonian, in particular the leading order XXZ terms, and it is not guaranteed that it would enhance the mobility. Since $\Gamma > 0$ and the product $\sigma_{i+1}^z \sigma_{i+2}^z$ is positive on trimer states, the overall sign of the process is also positive. As shown in the previous paragraph for the perturbative regime and in Fig. 2(a,b), XXZ trimers have an inverted band with positive hopping. Thus the correlated hopping process adds up constructively to them and leads to an enhancement of the mobility rather than a suppression. As a consequence, the effective group velocity of the trimer increases and the corresponding energy band becomes more dispersive. This effect is illustrated in Fig. 2(d), which compares the trimer dispersion for increasing values of Γ . The presence of the third-neighbor correlated hopping in Eq. (9) visibly increases the bandwidth of the trimer.

To complement the band structure analysis, we study trimer dynamics of the XXZ Hamiltonian under the WAHUA protocol discussed above in chains of $L = 17$ sites. We find that trimer propagation remains well-defined and consistent with the predictions of the second-order effective Hamiltonian (9), as long as $\Gamma \lesssim 0.01$ ($\omega/J_{nn} \gtrsim 8$). In this regime, we observe an enhancement of the trimer propagation velocity of approximately up to 30% compared to the undriven $\Gamma \rightarrow 0$ case. Despite the presence of $SO(2)$ -breaking terms, the dominating fast dynamics is dictated by the trimer light cone as we comment further below.

We support the above conclusions by monitoring the quantum walk dynamics of an initial product state $|i\rangle_T = |\dots \downarrow \uparrow_i \uparrow_{i+1} \uparrow_{i+2} \downarrow \dots\rangle$ using three complementary observables. First, we monitor the time evolution of the local magnetization, $n_i = (1 + \sigma_i^z)/2$, which reveals a coherent ballistic front that is consistent with the light cone velocity v_{\max} obtained from the effective theory Eq. (9), see Fig. 3(a). Second, we compute a 5-point trimer correlator, specifically designed to detect isolated three-spin bound states surrounded by spin-down spins [57, 58]:

$$\mathcal{T}_i(t) = \langle (1 - n_{i-2}) n_{i-1} n_i n_{i+1} (1 - n_{i+2}) \rangle. \quad (16)$$

This correlator clearly traces the same light-cone structure observed in the local magnetization, see Fig. 3(b). Finally, we quantify the total magnetization contained inside and outside the light-cone. We find that the magnetization outside the light-cone remains small and approximately constant while the magnetization inside the cone increase with time. This indicates that processes not conserving magnetization are dominantly

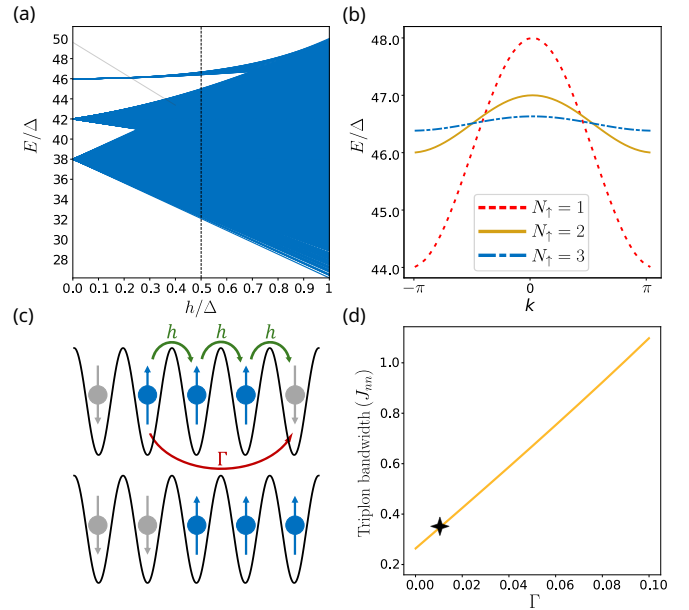


Figure 2: Trimer properties in the XXZ model and its Floquet corrections. (a) Energy spectrum of the 1D XXZ model (with closed boundary conditions) in the $N_\uparrow = 3$ sector for $L = 50$ sites as a function of h/Δ . The trimer band appears as a narrow, high-energy band separated from lower-energy scattering states for $h/\Delta \lesssim 2/3$. The vertical dashed black line marks the reference value $h/\Delta = 0.5$, corresponding to the value for the leading order XXZ terms in Eq. (9). (b) Comparison of the highest-energy bands of the XXZ model at $h/\Delta = 0.5$ across different magnetization sectors ($N_\uparrow = 1, 2$, and 3) highlighting the different dispersion of magnons, dimers and trimers. (c) Schematic illustration of the correlated third-neighbor hopping process contributing to trimer propagation in the effective Hamiltonian. (d) Bandwidth of the trimer band from Eq. (9) as a function of the Floquet parameter Γ . The black star marks the choice of $\Gamma = 0.01$, used throughout the main text.

slower than the trimer propagation and do not hinder the identification of its dynamics. Altogether, these observations suggest that symmetry-breaking processes do not dominate the dynamics as long as $\Gamma \lesssim 0.015$, allowing coherent trimer propagation to be resolved. For comparison, we also simulate the dynamics of a single magnon and a two-spin dimer under the same driven Hamiltonian, using initial states respectively given by $|\dots \downarrow \uparrow_i \downarrow \dots\rangle$ and $|\dots \downarrow \uparrow_i \uparrow_{i+1} \downarrow \dots\rangle$. In both cases we employ the same system size ($L = 17$), drive strength ($\Gamma = 0.01$), and closed boundary conditions used in the trimer case. The corresponding magnetization profiles, shown in Fig. 3(d,e), illustrate the faster propagation of these excitations compared to the trimer. We checked that the dynamics with closed boundary conditions is reproduced also for an open chain with a sufficiently large number of sites $L \geq 50$ to minimize boundary effects.

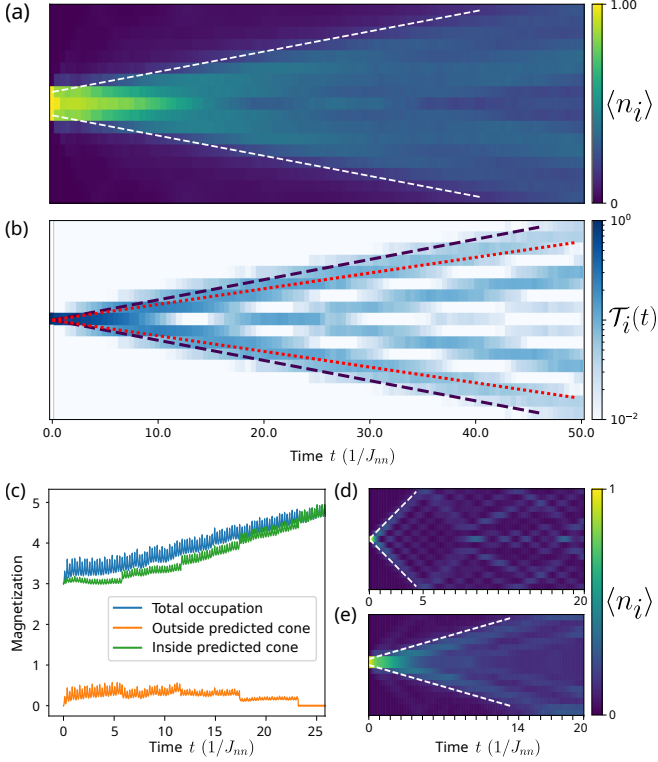


Figure 3: Time-resolved diagnostics of trimer propagation in a 17-site chain under the exact driven Hamiltonian with $\Gamma = 0.01$ and closed boundary conditions. (a) Local magnetization as a function of time, showing a clear light-cone structure emerging from a central trimer excitation. The effective light-cone (white dashed line) is obtained from the bound-state dispersion by extracting the maximum slope via finite differences over three adjacent k -points in the exact spectrum. (b) Time evolution of the trimer correlator $\mathcal{T}_i(t)$ showing ballistic behavior. The dashed dark line marks the effective light-cone velocity for $\Gamma = 0.01$ ($v \approx 0.173$), while the dotted red line shows the velocity for $\Gamma \rightarrow 0$ ($v \approx 0.130$) for comparison. (c) Time evolution of the magnetization $m = \sum_i n_i$ inside the light cone (green), outside of the cone (orange) and the total one (blue). The step-like structure of the curves arises the discrete nature of the lattice. (d) Magnetization profile of a propagating single-spin magnon and (e) of a dimer.

IV. LONG-RANGE AND HIGHER-DIMENSIONAL EFFECTS

In the previous sections, we have focused on trimer dynamics in one-dimensional systems with nearest-neighbor interactions. While this setup captures the essential physical mechanisms and allows for clear analytical treatment, it is important to address generalizations that bring the model closer to experimental platforms and open further directions. Here we consider two such extensions: the inclusion of long-range interactions and

the generalization to two-dimensional lattice geometries.

A. Long-range interactions

One of the most natural and experimentally relevant extensions concerns systems with long-range interactions as compared to the nearest-neighbor couplings considered above. In particular, platforms based on Rydberg atoms trapped in optical tweezers provide a natural setting for realizing spin models with tunable long-range dipolar interactions [11, 15, 59], while alternative realizations include magnetic dipolar atoms [60] and polar molecules [61, 62]. Rydberg systems implement an XY Hamiltonian, Eq. (2), through dipole-dipole exchange processes, and an external magnetic field determines the angular structure of the interactions. Specifically the atom-atom interactions in Eq. (2) scale as $J_{ij} = C_{dd}(1 - 3\cos^2\theta_{ij})/r_{ij}^3$, with θ_{ij} the angle between the magnetic field and the interatomic axis [63]. This provides a convenient knob to tune anisotropy in the atom-atom couplings as well as the sign. In this work, we consider lattice geometries (e.g. a one-dimensional chain or a two-dimensional lattice) for which we can choose the angle $\theta_{ij} = \pi/2$ for all pairs of atoms i and j and obtain isotropic dipolar interactions decaying as $1/r_{ij}^3$. More generally, one can however ask how the results of this work depend on the decay of the interactions with distance as $1/r^\alpha$, with $\alpha = 3$ being the dipolar case. This is motivated by the fact that properties of bound states can indeed strongly depend on the long-range tail [21, 64] and different platforms provide distinct and possibly tunable long-range couplings [65].

The Floquet analysis presented in previous sections can be extended in the presence of long-range couplings, leading to an effective model analogous to Eq. (9) but containing additional long-range interaction channels, including new terms that break $SO(2)$ (see Eq. B8). To probe the impact of these additional interactions on trimer dynamics we computed the maximum group velocity of the trimer band for various values of α and Floquet strengths Γ in the sector $N_\uparrow = 3$ (shown in Fig. 4(a)), thus restricting the analysis to the $SO(2)$ symmetric terms. We find that the trimer mobility substantially increases as α decreases, *i.e.* as interactions become longer-ranged, while the dynamics remains effectively bounded by a linear light cone [66]. Not only does the natural (zeroth-order) trimer velocity increases, but the additional enhancement due to second-order corrections is also amplified at low α values. This analysis is supported by real-time dynamics showing that the predicted velocity corresponds to an analogous propagation cone, see Fig. 4(b) for $\alpha = 3$. Specifically, we find that the Floquet drive induces an enhancement up to 60% faster than the undriven propagation. Furthermore, a comparison with the nearest-neighbor case studied in Fig. 3 shows a clear drastic improvement of the propagation time scale. Here the trimer reaches the

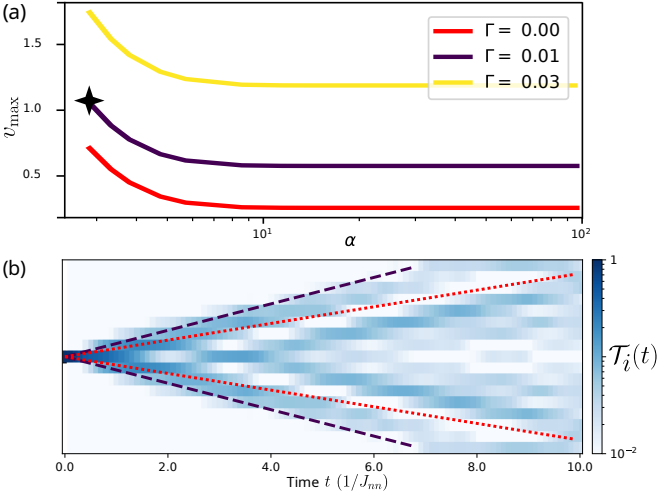


Figure 4: (a) Maximum trimer velocity $v_{\max} = \frac{\partial E_T(k)}{\partial k}$ evaluated from the exact-diagonalization spectrum of the generic H_{eff} up to $\mathcal{O}(1/\omega^2)$, see Eqs. (7), (8), including long-range couplings $J_{ij} \sim 1/r_{ij}^\alpha$ for $L = 17$, closed boundary conditions in the sector $N_\uparrow = 3$. The distance r_{ij} is taken as the minimal distance on the periodic chain. The lower cutoff $\alpha = 3$ corresponds to the dipolar case. The black star marks the choice of Γ and α used in section IV A. (b) Time evolution under the exact driven Hamiltonian of the trimer projection operator $\mathcal{T}_i(t)$ for $\Gamma = 0.01$ and $\alpha = 3$ (dipolar couplings). We observe an increase of $\sim 60\%$ in the speed of the excitations with respect to the $\Gamma \rightarrow 0$ case (red dotted line).

edge after 6 tunneling times J_{nn} , whereas in the nearest-neighbor case it was a much slower process requiring 45 tunneling times for a chain with 17 sites.

Recent experiments demonstrate that the characteristic interaction strengths and timescales assumed in this work are compatible with state-of-the-art Rydberg quantum simulators. For example, in the Rydberg implementation by Scholl et al. [54] and by Chen et al. [67] dynamics up to a few tunneling time (\hbar/J_{nn}) is achieved, which is within the range required by our findings as in Fig. 4.

B. Two-dimensional geometries

An issue of the discussion above is the breakdown of $SO(2)$ symmetry which yields excitations with different spin content to propagate. This effect is rooted in the energy cost of excitations, and specifically in the domain wall counting. Indeed, a string of n -spin up excitations always has approximately the same energy for any value of n . The effect of $H_{SO(2)}$ in Eq. (10) is to induce mixing of different magnetization sectors ($N_\uparrow = 3$ and $N_\uparrow = 7$) during the dynamics, without however hindering the identification of trimer dynamics for sufficiently small Γ .

A convenient strategy to suppress these processes is

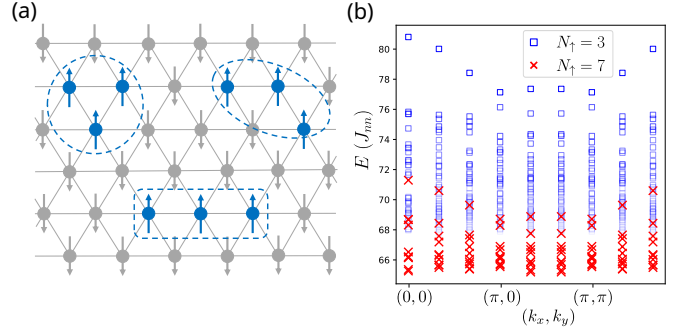


Figure 5: (a) Schematic representation of trimeric bound state geometries on a triangular lattice. (b) The spectrum of the effective Hamiltonian (see Eq. B8 in the Appendices) with $\Gamma = 0.015$ in a 2D triangular lattice of 36 sites with first neighbors couplings and closed boundary conditions along both directions. The plot shows energy levels in the $N_\uparrow = 3$ sector (blue squares) and the $N_\uparrow = 7$ sector (red crosses) along a momentum-space path in the 2D Brillouin zone. The trimer bands correspond to the 11 most energetic ones in the $N_\uparrow = 3$ sector. The highest trimer band appears as an isolated, high-energy branch, energetically well separated from both other $N_\uparrow = 3$ excitations and from higher-spin sectors like $N_\uparrow = 7$.

to bring the two magnetization sectors off resonance, for example by considering a two-dimensional geometry where the number of domain walls of trimers is different from other n -spin excitations. To be specific we focus on a triangular geometry with nearest-neighbor couplings, as depicted in Fig. 5(a), but other geometries can provide similar mechanisms with distinct features. As shown in the figure, there are different kinds of trimer excitations based on their geometric structure that have 12 and 14 domain walls. This provides an energy cost $\Delta E = 24-28J$ with respect to the fully polarized state. Instead, the 7-spin excitations have 18-30 domain walls with an energy cost $\Delta E = 36-60J$. The trimers are of three types: triangles (T) and linear (L) or chair-shaped (C) states, shown in Fig. 5(a). Notice that trimers T are not degenerate with trimers L and C due to the different count of domain walls. In Fig. 5(b), we show the ED spectrum of the Hamiltonian in Eq. (B8) of the Appendices for a small lattice 6×6 , where the two sectors $N_\uparrow = 3$ and $N_\uparrow = 7$ are plotted for $\Gamma = 0.015$. We notice that a trimer band survives and is quite isolated in the upper part of the spectrum. This corresponds to hybridized T trimers, namely superpositions of up and down triangles T, which are energetically off resonant from the $N_\uparrow = 7$ manifold as well as scattering states.

A full time-dependent analysis in 2D requires higher computational resources or strategies compared to those discussed so far, and is thus beyond the scope of this work. However, the results shown above strongly suggest that the trimer propagation should remain more stable against the $SO(2)$ breaking process in such geometries.

This makes 2D triangular arrays a promising candidate for the realization of multiparticle bound state transport, as shown from recent experimental implementations [68, 69]. Moreover, the multiband structure of trimers in lattices different from one-dimensional chains offers an opportunity to investigate non-trivial bound state dynamics with emergent topological properties [28, 56].

V. CONCLUSIONS

In this work, we have explored the emergence and dynamics of trimer bound states in periodically driven spin models engineered via Rydberg atom arrays. By applying a WAHUHA-type Floquet sequence to an underlying dipolar XY Hamiltonian, we obtained an effective XYZ model with tunable anisotropies and second-order corrections that include correlated hopping and multispin interactions.

Our analytical and numerical results demonstrate that second-order Floquet terms enhance trimer mobility in a certain limit of the protocol that approximately conserves magnetization, enabling longer-range correlated motion. Despite the presence of terms breaking magnetization conservation appearing in the Floquet second-order expansion, we find that trimer dynamics remains robust in small systems and even in larger chains provided that the driving frequency is sufficiently high. Moreover, we show that long-range interactions and two-dimensional geometries further stabilize the bound state propagation by energetically separating trimers from other kinds of multiparticle excitations.

These findings provide a new route to engineer and study multiparticle bound states in programmable quantum simulators. The parameter regimes considered are directly relevant to current experimental platforms based on Rydberg atoms, where Floquet periods and interaction scales naturally fall in the range of few microseconds. Furthermore, recent advances with polar molecules also provide an alternative setting for our findings [70]. Our work provides further support in exploring beyond-leading order analyses of Floquet engineered Rydberg systems to investigate non-equilibrium dynamics of many-body quantum states. An interesting perspective is to analyze how alternative pulse sequences [71] yield interaction channels distinct from the ones analyzed here, which can significantly affect the mobility of multiparticle states.

VI. ACKNOWLEDGMENTS

Acknowledgements. This work has received funding under the Horizon Europe programme HORIZON-CL4-2022-QUANTUM-02-SGA via the project 101113690 (PASQuanS2.1), the European Union-NextGenerationEU within the National Center for HPC, Big Data and Quantum Computing (Project No.

CN00000013, CN1 Spoke 10: ‘Quantum Computing’), and has been supported by the INFN project Iniziativa Specifica IS-Quantum, the Italian Ministry of University and Research via the Excellence grant 2023-2027 “Quantum Frontiers”, the Rita Levi-Montalcini program. L.M. has been supported by the project “BALANCY” under the MSCA Seal of Excellence @Unipd programme.

Appendix A: Details of Floquet

We consider a generic time-dependent Hamiltonian composed of a static and a periodic contribution,

$$H'(t) = H_0 + W'(t), \quad (\text{A1})$$

where H_0 is time independent and $W'(t)$ is a periodic operator with period $T = 2\pi/\omega$. The periodic part can be expanded in a Fourier series as

$$W'(t) = \sum_{n \geq 1} \left(V^{(n)} e^{in\omega t} + V^{(n)\dagger} e^{-in\omega t} \right). \quad (\text{A2})$$

As a concrete example, we consider the rotated Hamiltonian $H'(t)$ defined in Eq. (4). This Hamiltonian can be decomposed into a time-independent part H_0 , given explicitly in Eq. (6), and a time-periodic contribution whose Fourier components read

$$V^{(n)} = \sum_{i \neq j} \frac{J_{i,j}}{2\pi n} \left[\sin(n\omega(\tau_1 + \tau_2)) (\sigma_i^x \sigma_j^x - \sigma_i^y \sigma_j^y) + \sin(n\omega\tau_1) (\sigma_i^y \sigma_j^y - \sigma_i^z \sigma_j^z) \right], \quad (\text{A3})$$

with $V^{(n)\dagger} = V^{(n)}$ and $V^{(0)} \equiv 0$. Within the high-frequency Floquet formalism, the effective Hamiltonian governing the stroboscopic dynamics over one driving period is given by

$$\begin{aligned} H_{\text{eff}} = H_0 &+ \frac{1}{\omega} \sum_{n=1}^{\infty} \frac{1}{n} [V^{(n)}, V^{(n)\dagger}] \\ &+ \frac{1}{2\omega^2} \sum_{n=1}^{\infty} \frac{1}{n^2} [[V^{(n)}, H_0], V^{(n)\dagger}] \\ &+ \frac{1}{\omega^2} \sum_{n,m=1}^{\infty} \frac{1}{n(n+m)} [V^{(n)}, [V^{(m)}, V^{(n+m)\dagger}]] \\ &+ \text{h.c.} + \mathcal{O}(1/\omega^3). \end{aligned} \quad (\text{A4})$$

In the present case, since $V^{(n)} = V^{(n)\dagger}$, the first-order correction in $1/\omega$ vanishes identically. As a result, the leading nontrivial corrections to H_0 arise at second order in the inverse driving frequency and scale as $1/\omega^2$. This expansion follows the standard high-frequency Floquet formalism described in Ref. [35].

Appendix B: Second order coefficients

As shown in Appendix A, the leading nonvanishing corrections to the effective Hamiltonian arise at second order in the high-frequency expansion and scale as $1/\omega^2$. In this appendix we provide the explicit expressions of the corresponding second-order effective Hamiltonian, which consists of both two-spin and four-spin interaction terms ($H_{\text{eff}}^{(2)}/\omega^2 = H^{2\sigma} + H^{4\sigma}$), given in Eqs. (7) and (8). The coefficients appearing in the two-spin second-order Hamiltonian $H^{2\sigma}$ are given by

$$\begin{aligned}\mathcal{J}_{j,k}^x &= \frac{8}{\omega^2\pi^2} \sum_{i \neq j,k} \sum_{m=0}^{\infty} \frac{J_{i,j} \left(\Lambda_{kji}^{(n,m)} A_z^{(n)} - \Lambda_{kij}^{(n,m)} A_y^{(n)} \right)}{n^2(n+m)^2}, \\ \mathcal{J}_{j,k}^y &= \frac{8}{\omega^2\pi^2} \sum_{i \neq j,k} \sum_{m=0}^{\infty} \frac{J_{i,j} \left(\Lambda_{ikj}^{(n,m)} A_x^{(n)} - \Lambda_{jki}^{(n,m)} A_z^{(n)} \right)}{n^2(n+m)^2}, \\ \mathcal{J}_{j,k}^z &= \frac{8}{\omega^2\pi^2} \sum_{i \neq j,k} \sum_{m=0}^{\infty} \frac{J_{i,j} \left(\Lambda_{jik}^{(n,m)} A_y^{(n)} - \Lambda_{ijk}^{(n,m)} A_x^{(n)} \right)}{n^2(n+m)^2}.\end{aligned}\quad (B1)$$

Here $J_{i,j}$ denotes the native dipolar couplings introduced in Eq. (2). The remaining coefficients entering the above expressions are defined as

$$\begin{aligned}A_x^{(n)} &= \sin[n\omega(\tau_1 + \tau_2)], \\ A_y^{(n)} &= \sin(n\omega\tau_1) - \sin[n\omega(\tau_1 + \tau_2)], \\ A_z^{(n)} &= -\sin(n\omega\tau_1).\end{aligned}\quad (B2)$$

The coefficients $\Lambda_{ijk}^{(n,m)}$ take different forms depending on whether $m = 0$ or $m \neq 0$. For $m = 0$ they read

$$\begin{aligned}\Lambda_{ijk}^{(n,0)} &= \left[A_z^{(n)}(\tau_1 + \tau_2) - A_x^{(n)}(\tau_2 + \tau_3) \right] \frac{J_{i,j} J_{j,k}}{T} \\ &+ \left[A_x^{(n)}(\tau_1 + \tau_3) - A_y^{(n)}(\tau_1 + \tau_2) \right] \frac{J_{i,k} J_{k,j}}{T} \\ &+ \left[A_y^{(n)}(\tau_2 + \tau_3) - A_z^{(n)}(\tau_1 + \tau_3) \right] \frac{J_{j,i} J_{i,k}}{T},\end{aligned}\quad (B3)$$

whereas for $m \neq 0$ one finds

$$\begin{aligned}\Lambda_{ijk}^{(n,m)} &= \left[A_z^{(n+m)} A_x^{(m)} - A_x^{(n+m)} A_z^{(m)} \right] \frac{J_{i,j} J_{j,k}}{\pi m} \\ &+ \left[A_x^{(n+m)} A_y^{(m)} - A_y^{(n+m)} A_x^{(m)} \right] \frac{J_{i,k} J_{k,j}}{\pi m} \\ &+ \left[A_y^{(n+m)} A_z^{(m)} - A_z^{(n+m)} A_y^{(m)} \right] \frac{J_{j,i} J_{i,k}}{\pi m}.\end{aligned}\quad (B4)$$

The four-spin contribution to the second-order effec-

tive Hamiltonian can be originally written as

$$\begin{aligned}H^{4\sigma} &= \sum_{h \neq i \neq j \neq k} \left(c_{hijk}^{yz} \sigma_h^y \sigma_i^y \sigma_j^z \sigma_k^z + c_{hijk}^{zx} \sigma_h^z \sigma_i^z \sigma_j^x \sigma_k^x \right. \\ &\quad \left. + c_{hijk}^{xy} \sigma_h^x \sigma_i^x \sigma_j^y \sigma_k^y \right),\end{aligned}\quad (B5)$$

where the coefficients are given by

$$\begin{aligned}c_{hijk}^{yz} &= \frac{8}{\omega^2\pi^2} \sum_{m=0}^{\infty} \frac{J_{h,j} \left(\Lambda_{hik}^{(n,m)} A_z^{(n)} - \Lambda_{jik}^{(n,m)} A_y^{(n)} \right)}{n^2(n+m)^2}, \\ c_{hijk}^{zx} &= \frac{8}{\omega^2\pi^2} \sum_{m=0}^{\infty} \frac{J_{h,j} \left(\Lambda_{khi}^{(n,m)} A_x^{(n)} - \Lambda_{kji}^{(n,m)} A_z^{(n)} \right)}{n^2(n+m)^2}, \\ c_{hijk}^{xy} &= \frac{8}{\omega^2\pi^2} \sum_{m=0}^{\infty} \frac{J_{h,j} \left(\Lambda_{ikh}^{(n,m)} A_y^{(n)} - \Lambda_{ikj}^{(n,m)} A_x^{(n)} \right)}{n^2(n+m)^2}.\end{aligned}\quad (B6)$$

The spin operators appearing in $H^{4\sigma}$ are symmetric under the exchanges $h \leftrightarrow i$ and $j \leftrightarrow k$. It is therefore convenient to introduce symmetrized coefficients

$$C_{hi;jk} = c_{hijk} + c_{hikj} + c_{ihjk} + c_{ihkj}, \quad (B7)$$

in terms of which the four-spin Hamiltonian takes the compact form reported in Eq. (8). The restricted summation in that equation, together with the condition $\{h, i\} \cap \{j, k\} = \emptyset$, accounts for the fact that the coefficients are not symmetric under the exchange of the two index pairs $(h, i) \leftrightarrow (j, k)$.

The emergence of a pseudo- $SO(2)$ symmetry at second order requires the conditions $\mathcal{J}_{j,k}^x = \mathcal{J}_{j,k}^y$ for all j, k and $C_{hi;jk}^{yz} = C_{jk;hi}^{zx}$ for all h, i, j, k . These constraints imply $A_z^{(n)} = 0$ and $A_y^{(n)} = -A_x^{(n)}$, which can only be satisfied in the limit $\tau_1 \rightarrow 0$ (see Fig. 6). This choice must be combined with the condition $\tau_2 = \tau_3$, which enforces an $SO(2)$ symmetry already at zeroth order.

With this choice of parameters, the definitions of the coefficients simplify dramatically: one can verify that all quantities $\Lambda_{ijk}^{(n,m)}$ with $m \neq 0$, defined in Eq. (B4), vanish. The remaining sums over n (with $m = 0$) reduce to

$$\frac{8}{(\omega\pi)^2} \sum_{n=1}^{\infty} \frac{(A_x^{(n)})^2}{n^4} = \frac{8}{(\omega\pi)^2} \sum_{n=1}^{\infty} \frac{\sin^2(n\pi/2)}{n^4} = \frac{1}{12} \left(\frac{\pi}{\omega} \right)^2,$$

up to products of the couplings J . Introducing the parameter $\Gamma \equiv \frac{1}{6} \left(\frac{J_{nn}\pi}{\omega} \right)^2$, the Hamiltonian (A4) can be cast in the form $H_{\text{eff}} = \sum_{jk} H_{j>k} + \mathcal{O}(1/\omega^3)$, with:

$$\begin{aligned}
H_{j>k} = & J_{j,k} (\sigma_j^+ \sigma_k^- + \sigma_j^- \sigma_k^+ + \sigma_j^z \sigma_k^z) \\
& - \frac{\Gamma}{2J_{\text{nn}}^2} \sum_{i \neq j,k} \left(J_{i,j}^2 J_{j,k} + J_{i,k}^2 J_{j,k} - 2J_{i,j} J_{i,k} J_{j,k} - J_{i,j}^2 J_{i,k} - J_{i,k}^2 J_{i,j} \right) (\sigma_j^+ \sigma_k^- + \sigma_j^- \sigma_k^+) \\
& - \frac{\Gamma}{2J_{\text{nn}}^2} \sum_{i \neq j,k} \left(J_{i,j}^2 J_{j,k} + J_{i,j}^2 J_{i,k} + J_{i,k}^2 J_{j,k} + J_{i,k}^2 J_{i,j} - 2J_{i,j} J_{i,k} J_{j,k} \right) \sigma_j^z \sigma_k^z \\
& - \frac{\Gamma}{J_{\text{nn}}^2} \sum_{h>i} \left[J_{h,j} J_{i,k} J_{h,k} + J_{h,k} J_{i,j} J_{h,j} + J_{i,j} J_{h,k} J_{i,k} + J_{i,k} J_{h,j} J_{i,j} \right. \\
& \quad \left. + 2(J_{h,i} J_{h,j} J_{h,k} + J_{i,j} J_{h,i} J_{i,k} - J_{h,j} J_{h,i} J_{i,k} - J_{h,k} J_{h,i} J_{i,j}) \right] \sigma_h^z \sigma_i^z (\sigma_j^+ \sigma_k^- + \sigma_j^- \sigma_k^+) \\
& + \frac{\Gamma}{2J_{\text{nn}}^2} \sum_{h>i} \left[+ J_{h,j} J_{i,k} J_{h,k} + J_{h,k} J_{i,j} J_{h,j} + J_{i,j} J_{h,k} J_{i,k} + J_{i,k} J_{h,j} J_{i,j} \right. \\
& \quad \left. + J_{h,j} J_{h,i} J_{i,k} + J_{h,k} J_{h,i} J_{i,j} + J_{h,j} J_{i,k} J_{j,k} + J_{h,k} J_{i,j} J_{j,k} \right. \\
& \quad \left. - (J_{h,i} J_{h,j} J_{h,k} + J_{i,j} J_{h,i} J_{i,k} + J_{h,j} J_{i,j} J_{j,k} + J_{h,k} J_{i,k} J_{j,k}) \right] \sigma_h^x \sigma_i^x \sigma_j^y \sigma_k^y. \tag{B8}
\end{aligned}$$

This expression remains valid for arbitrary lattice geometries and interaction profiles $J_{i,j}$. Specializing to a nearest-neighbor chain yields Eqs. (9) and (10).

A convenient alternative set of parameters is obtained by taking $\tau_3 \rightarrow 0$ while imposing $\tau_1 = \tau_2$ (that is, $A_x^{(n)} = 0$ and $A_z^{(n)} = -A_y^{(n)}$). In this case the two central pulses with phases $\phi = -\pi/2$ and $\phi = +\pi/2$ become coincident at mid period and cancel each other, so that the protocol again reduces to a two-pulse sequence per period, now consisting of $\phi = 0$ and $\phi = \pi$ applied at $t = T/4$ and $t = 3T/4$. Crucially, this implementation avoids the need for a pulse at $t = 0$, leaving a time window of $T/4$ after the quench before the first pulse is applied. The resulting effective Hamiltonian is equivalent to the one discussed above up to a global spin rotation (i.e., a relabeling of spin axes); in this paper we nonetheless adopt the convention in which the pseudo- $SO(2)$ symmetry lies in the x - y plane, which is the most common choice in the literature.

Appendix C: Floquet theory benchmark

We validate the second-order effective Floquet Hamiltonian (9) with closed boundary conditions by comparing its dynamics with the exact one obtained via the time-dependent evolution via the full Hamiltonian (1). This comparison focuses on the magnetization dynamics starting from a trimer state, i.e. a state in which three neighboring spins are flipped on top of a fully polarized background.

For relatively small system sizes (up to 7 spins) the two

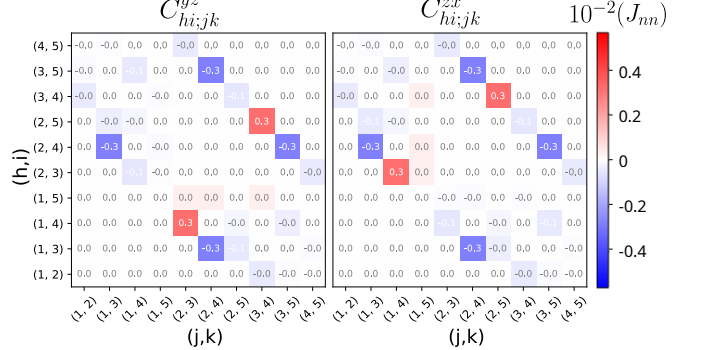


Figure 6: Visualization of the four-body interaction coefficients $C_{hi;jk}^{yz}$ and $C_{hi;jk}^{zx}$ appearing in $H^{4\sigma}$ (Eq. 8) for a 5-site chain with dipolar couplings ($J_{ij} \propto 1/|i - j|^3$), evaluated at $\Gamma = 0.01$. The driving protocol is characterized by WAHUHA parameters $\tau_1 = 0$, $\tau_2/T = 0.33$, and $\tau_3/T = 0.17$. The y -axis of each subplot labels all index pairs (h, i) and the x -axis all pairs (j, k) . The perfect equivalence between $C_{hi;jk}^{yz}$ and $C_{jk;hi}^{zx}$ across the plots confirms the emergence of the pseudo- $SO(2)$ symmetry when $\tau_1 \rightarrow 0$, as discussed in Appendix B.

evolutions show excellent agreement even at moderate driving frequencies $\omega/J_{\text{nn}} \sim 6$. In this regime, the parameter Γ reaches values as high as 0.02 without compromising the accuracy of the effective description (9) (see Fig 7(a)).

For larger systems, higher order terms become quickly effective as they include couplings that are more delocalized among several spins along the chain. This restricts

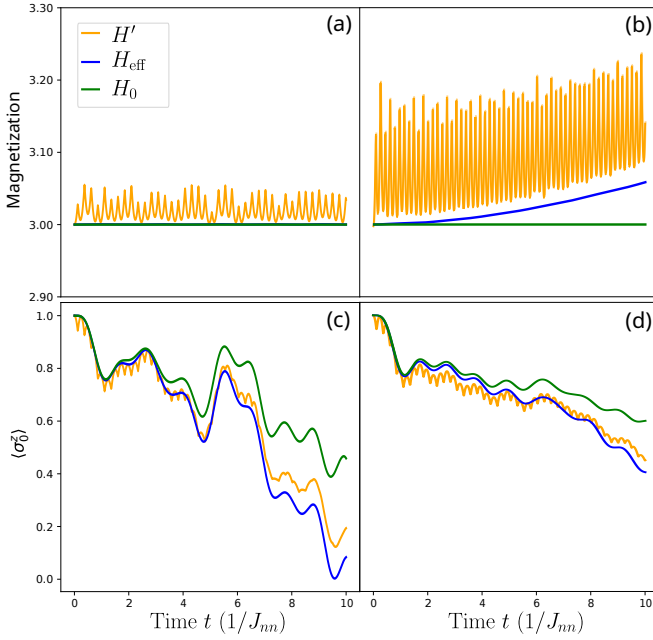


Figure 7: Time evolution of global (top panels) and local magnetization (bottom panels) in finite spin chains with $L = 7$ (left panels) and $L = 15$ (right panels), starting from a trimer initial state $\langle N_{\uparrow} \rangle = 3$. In all panels, we compare the dynamics generated by the exact driven Hamiltonian (orange), the second-order effective Hamiltonian (Eqs. (9)-(10) in the main text) (blue), and the leading order XXZ model (green line). The driving parameters are chosen such that $\Gamma = 0.01$ for the $L = 7$ panels (a)-(c) and $\Gamma = 0.005$ for the $L = 15$ panels (b)-(d).

the practical advantage of including only second order corrections in a smaller range of Γ s.

For example, when studying the behavior of total magnetization, the effective Hamiltonian (9) already includes a symmetry-breaking term. However, its presence alone does not fully explain the magnetization variation in long chains. Nevertheless, reducing Γ yields an accurate effective description once again (see Fig. 7(b)).

On the other hand, although discrepancies in magnetization become apparent for large systems at low frequencies, other observables are well captured by the effective model (Fig. 7(d)), and the light-cone structure remains qualitatively similar, indicating agreement in the propagation of correlations (Fig. 3).

[1] S. Sachdev, *Quantum phases of matter* (Cambridge University Press, 2023).

[2] I. M. Georgescu, S. Ashhab, and F. Nori, *Rev. Mod. Phys.* **86**, 153 (2014).

[3] L.-M. Duan, E. Demler, and M. D. Lukin, *Phys. Rev. Lett.* **91**, 090402 (2003).

[4] T. Fukuhara, P. Schauß, M. Endres, S. Hild, M. Cheneau, I. Bloch, and C. Gross, *Nature* **502**, 76 (2013).

[5] D. Greif, T. Uehlinger, G. Jotzu, L. Tarruell, and T. Esslinger, *Science* **340**, 1307 (2013).

[6] M. Boll, T. A. Hilker, G. Salomon, A. Omran, J. Nespolo, L. Pollet, I. Bloch, and C. Gross, *Science* **353**, 1257 (2016).

[7] A. Mazurenko, C. S. Chiu, G. Ji, M. F. Parsons, M. Kanász-Nagy, R. Schmidt, F. Grusdt, E. Demler, D. Greif, and M. Greiner, *Nature* **545**, 462 (2017).

[8] C. Trefzger, C. Menotti, B. Capogrosso-Sansone, and M. Lewenstein, *Journal of Physics B: Atomic, Molecular and Optical Physics* **44**, 193001 (2011).

[9] M. A. Baranov, M. Dalmonte, G. Pupillo, and P. Zoller, *Chemical Reviews* **112**, 5012 (2012).

[10] M. Saffman, T. G. Walker, and K. Mølmer, *Reviews of Modern Physics* **82**, 2313 (2010).

[11] A. Browaeys and T. Lahaye, *Nature Physics* **16**, 132 (2020), publisher: Nature Publishing Group.

[12] V. Lienhard, P. Scholl, S. Weber, D. Barredo, S. De Léséleuc, R. Bai, N. Lang, M. Fleischhauer, H. P. Büchler, T. Lahaye, and A. Browaeys, *Physical Review X* **10**, 021031 (2020).

[13] A. Keesling, A. Omran, H. Levine, H. Bernien, H. Pichler, S. Choi, R. Samajdar, S. Schwartz, P. Silvi, S. Sachdev, P. Zoller, M. Endres, M. Greiner, V. Vuletić, and M. D. Lukin, *Nature* **568**, 207 (2019).

[14] S. Ebadi, T. T. Wang, H. Levine, A. Keesling, G. Semeghini, A. Omran, D. Bluvstein, R. Samajdar, H. Pichler, W. W. Ho, S. Choi, S. Sachdev, M. Greiner, V. Vuletić, and M. D. Lukin, *Nature* **595**, 227 (2021).

[15] S. de Léséleuc, V. Lienhard, P. Scholl, D. Barredo, S. Weber, N. Lang, H. P. Büchler, T. Lahaye, and A. Browaeys, *Science* **365**, 775 (2019).

[16] G. Semeghini, H. Levine, A. Keesling, S. Ebadi, T. T. Wang, D. Bluvstein, R. Verresen, H. Pichler, M. Kalinowski, R. Samajdar, A. Omran, S. Sachdev, A. Vishwanath, M. Greiner, V. Vuletić, and M. D. Lukin, *Science* **374**, 1242 (2021).

[17] H. Bernien, S. Schwartz, A. Keesling, H. Levine, A. Omran, H. Pichler, S. Choi, A. S. Zibrov, M. Endres, M. Greiner, V. Vuletić, and M. D. Lukin, *Nature* **551**,

579 (2017).

[18] T. Manovitz, S. H. Li, S. Ebadi, R. Samajdar, A. A. Geim, S. J. Evered, D. Bluvstein, H. Zhou, N. U. Koyluoglu, J. Feldmeier, P. E. Dolgirev, N. Maskara, M. Kalinowski, S. Sachdev, D. A. Huse, M. Greiner, V. Vuletić, and M. D. Lukin, *Nature* **638**, 86 (2025).

[19] M. Ganahl, E. Rabel, F. H. L. Essler, and H. G. Evertz, *Phys. Rev. Lett.* **108**, 077206 (2012).

[20] F. Letscher and D. Petrosyan, *Phys. Rev. A* **97**, 043415 (2018).

[21] T. Macrì, L. Lepori, G. Pagano, M. Lewenstein, and L. Barbiero, *Physical Review B* **104**, 214309 (2021).

[22] F. Kranzl, S. Birnkammer, M. K. Joshi, A. Bastianello, R. Blatt, M. Knap, and C. F. Roos, *Phys. Rev. X* **13**, 031017 (2023).

[23] K. Kim, F. Yang, K. Mølmer, and J. Ahn, *Phys. Rev. X* **14**, 011025 (2024).

[24] K. Winkler, G. Thalhammer, F. Lang, R. Grimm, J. Hecker Denschlag, A. J. Daley, A. Kantian, H. P. Büchler, and P. Zoller, *Nature* **441**, 853 (2006).

[25] M. E. Tai, A. Lukin, M. Rispoli, R. Schittko, T. Menke, Dan Borgnia, P. M. Preiss, F. Grusdt, A. M. Kaufman, and M. Greiner, *Nature* **546**, 519 (2017).

[26] M. Valiente and D. Petrosyan, *Journal of Physics B: Atomic, Molecular and Optical Physics* **42**, 121001 (2009).

[27] P. Weckesser, K. Srakaew, T. Blatz, D. Wei, D. Adler, S. Agrawal, A. Bohrdt, I. Bloch, and J. Zeiher, *Science* **390**, 849 (2025).

[28] G. Salerno, G. Palumbo, N. Goldman, and M. Di Liberto, *Phys. Rev. Res.* **2**, 013348 (2020).

[29] W.-H. Li, A. Dhar, X. Deng, and L. Santos, *Phys. Rev. A* **103**, 043331 (2021).

[30] G. Misguich, K. Mallick, and P. L. Krapivsky, *Phys. Rev. B* **96**, 195151 (2017).

[31] F. M. Surace, P. P. Mazza, G. Giudici, A. Lerose, A. Gambassi, and M. Dalmonte, *Phys. Rev. X* **10**, 021041 (2020).

[32] L. Pavešić, D. Jaschke, and S. Montangero, *Phys. Rev. B* **111**, L140305 (2025).

[33] D. González-Cuadra, M. Hamdan, T. V. Zache, B. Braverman, M. Kornjača, A. Lukin, S. H. Cantú, F. Liu, S.-T. Wang, A. Keesling, M. D. Lukin, P. Zoller, and A. Bylinskii, *Nature* **642**, 321 (2025).

[34] M. Kormos, M. Collura, G. Takács, and P. Calabrese, *Nature Physics* **13**, 246 (2017).

[35] N. Goldman and J. Dalibard, *Physical Review X* **4**, 031027 (2014).

[36] A. Eckardt, *Rev. Mod. Phys.* **89**, 011004 (2017).

[37] A. Eckardt, C. Weiss, and M. Holthaus, *Phys. Rev. Lett.* **95**, 260404 (2005).

[38] A. Zenesini, H. Lignier, D. Ciampini, O. Morsch, and E. Arimondo, *Phys. Rev. Lett.* **102**, 100403 (2009).

[39] M. Aidelsburger, M. Atala, S. Nascimbène, S. Trotzky, Y.-A. Chen, and I. Bloch, *Phys. Rev. Lett.* **107**, 255301 (2011).

[40] J. Struck, C. Ölschläger, M. Weinberg, P. Hauke, J. Simonet, A. Eckardt, M. Lewenstein, K. Sengstock, and P. Windpassinger, *Phys. Rev. Lett.* **108**, 225304 (2012).

[41] N. Goldman, G. Juzeliūnas, P. Öhberg, and I. B. Spielman, *Reports on Progress in Physics* **77**, 126401 (2014).

[42] D. A. Abanin, W. De Roeck, and F. m. c. Huvveneers, *Phys. Rev. Lett.* **115**, 256803 (2015).

[43] N. Goldman, J. C. Budich, and P. Zoller, *Nature Physics* **12**, 639 (2016).

[44] N. R. Cooper, J. Dalibard, and I. B. Spielman, *Rev. Mod. Phys.* **91**, 015005 (2019).

[45] A. Rapp, X. Deng, and L. Santos, *Phys. Rev. Lett.* **109**, 203005 (2012).

[46] M. D. Liberto, C. E. Creffield, G. I. Japaridze, and C. M. Smith, *Phys. Rev. A* **89**, 013624 (2014).

[47] L. Zhao, M. D. K. Lee, M. M. Aliyu, and H. Loh, *Nature Communications* **14**, 7128 (2023).

[48] N. U. Koyluoglu, N. Maskara, J. Feldmeier, and M. D. Lukin, *Phys. Rev. Lett.* **135**, 113603 (2025).

[49] M. Kalinowski, N. Maskara, and M. D. Lukin, *Phys. Rev. X* **13**, 031008 (2023).

[50] B.-Y. Sun, N. Goldman, M. Aidelsburger, and M. Bükov, *PRX Quantum* **4**, 020329 (2023).

[51] S. J. Evered, M. Kalinowski, A. A. Geim, T. Manovitz, D. Bluvstein, S. H. Li, N. Maskara, H. Zhou, S. Ebadi, M. Xu, *et al.*, *Nature* **645**, 341 (2025).

[52] J. S. Waugh, L. M. Huber, and U. Haeberlen, *Physical Review Letters* **20**, 180 (1968).

[53] S. Geier, N. Thaicharoen, C. Hainaut, T. Franz, A. Salzinger, A. Tebben, D. Grimshandl, G. Zürn, and M. Weidmüller, *Science* **374**, 1149 (2021).

[54] P. Scholl, H. J. Williams, G. Bornet, F. Wallner, D. Barredo, L. Henriet, A. Signoles, C. Hainaut, T. Franz, S. Geier, *et al.*, *PRX Quantum* **3**, 020303 (2022).

[55] M. Valiente, D. Petrosyan, and A. Saenz, *Phys. Rev. A* **81**, 011601 (2010).

[56] G. Giudice, F. M. Surace, H. Pichler, and G. Giudice, *Phys. Rev. B* **106**, 195155 (2022).

[57] P. M. Preiss, R. Ma, M. E. Tai, A. Lukin, M. Rispoli, P. Zupancic, Y. Lahini, R. Islam, and M. Greiner, *Science* **347**, 1229 (2015).

[58] A. Rapp, X. Deng, and L. Santos, *Physical Review Letters* **109**, 203005 (2012).

[59] S. De Léséleuc, D. Barredo, V. Lienhard, A. Browaeys, and T. Lahaye, *Physical Review Letters* **119**, 053202 (2017).

[60] L. Chomaz, I. Ferrier-Barbut, F. Ferlaino, B. Laburthe-Tolra, B. L. Lev, and T. Pfau, *Reports on Progress in Physics* **86**, 026401 (2022).

[61] A. Micheli, G. K. Brennen, and P. Zoller, *Nature Physics* **2**, 341 (2006).

[62] S. L. Cornish, M. R. Tarbutt, and K. R. A. Hazzard, *Nature Physics* **20**, 730 (2024).

[63] S. Ravets, H. Labuhn, D. Barredo, T. Lahaye, and A. Browaeys, *Phys. Rev. A* **92**, 020701 (2015).

[64] M. Teçer, M. Di Liberto, P. Silvi, S. Montangero, F. Romanato, and G. Calajó, *Phys. Rev. Lett.* **132**, 163602 (2024).

[65] N. Defenu, T. Donner, T. Macrì, G. Pagano, S. Ruffo, and A. Trombettoni, *Rev. Mod. Phys.* **95**, 035002 (2023).

[66] M. Foss-Feig, Z.-X. Gong, C. W. Clark, and A. V. Gorshkov, *Phys. Rev. Lett.* **114**, 157201 (2015).

[67] C. Chen, G. Emperauger, G. Bornet, F. Caleca, B. Gély, M. Bintz, S. Chatterjee, V. Liu, D. Barredo, N. Y. Yao, T. Lahaye, F. Mezzacapo, T. Roscilde, and A. Browaeys, *Science* **389**, 483 (2025).

[68] P. Scholl, M. Schuler, H. J. Williams, A. A. Eberharter, D. Barredo, K.-N. Schymik, V. Lienhard, L.-P. Henry, T. C. Lang, T. Lahaye, A. M. Läuchli, and A. Browaeys,

[Nature](#) **595**, 233 (2021), publisher: Nature Publishing Group.

[69] M. Qiao, R. Martin, L. Homeier, I. Morera, B. Gély, L. Klein, Y. T. Chew, D. Barredo, T. Lahaye, E. Demler, *et al.*, [arXiv preprint arXiv:2510.17183](#) (2025).

[70] C. Miller, A. N. Carroll, J. Lin, H. Hirzler, H. Gao, H. Zhou, M. D. Lukin, and J. Ye, [Nature](#) **633**, 332 (2024).

[71] H. Zhou, H. Gao, N. T. Leitao, O. Makarova, I. Cong, A. M. Douglas, L. S. Martin, and M. D. Lukin, [Phys. Rev. X](#) **14**, 031017 (2024).